NeuroImage 59 (2012) 2110–2123

Contents lists available at SciVerse ScienceDirect

NeuroImage

journal homepage: www.elsevier.com/locate/ynimg

Regional electric field induced by electroconvulsive therapy in a realistic finite element head model: Influence of white matter anisotropic conductivity

Won Hee Lee [a,b], Zhi-De Deng [b,c], Tae-Seong Kim [d], Andrew F. Laine [a], Sarah H. Lisanby [b,e], Angel V. Peterchev [b,f,*]

[a] Department of Biomedical Engineering, Columbia University, New York, NY 10027, USA
[b] Department of Psychiatry and Behavioral Sciences, Duke University, Durham, NC 27710, USA
[c] Department of Electrical Engineering, Columbia University, New York, NY 10027, USA
[d] Department of Biomedical Engineering, Kyung Hee University, Yongin, Gyeonggi, Republic of Korea
[e] Department of Psychology & Neuroscience, Duke University, Durham, NC 27710, USA
[f] Department of Biomedical Engineering and Department of Electrical and Computer Engineering, Duke University, Durham, NC 27710, USA

ARTICLE INFO

Article history:
Received 16 July 2011
Revised 14 September 2011
Accepted 10 October 2011
Available online 18 October 2011

Keywords:
Electroconvulsive therapy
Finite element method
Computational model
White matter anisotropy
Electric field
Magnetic resonance imaging
Brain stimulation

ABSTRACT

We present the first computational study investigating the electric field (E-field) strength generated by various electroconvulsive therapy (ECT) electrode configurations in specific brain regions of interest (ROIs) that have putative roles in the therapeutic action and/or adverse side effects of ECT. This study also characterizes the impact of the white matter (WM) conductivity anisotropy on the E-field distribution. A finite element head model incorporating tissue heterogeneity and WM anisotropic conductivity was constructed based on structural magnetic resonance imaging (MRI) and diffusion tensor MRI data. We computed the spatial E-field distributions generated by three standard ECT electrode placements including bilateral (BL), bifrontal (BF), and right unilateral (RUL) and an investigational electrode configuration for focal electrically administered seizure therapy (FEAST). The key results are that (1) the median E-field strength over the whole brain is 3.9, 1.5, 2.3, and 2.6 V/cm for the BL, BF, RUL, and FEAST electrode configurations, respectively, which coupled with the broad spread of the BL E-field suggests a biophysical basis for observations of superior efficacy of BL ECT compared to BF and RUL ECT; (2) in the hippocampi, BL ECT produces a median E-field of 4.8 V/cm that is 1.5–2.8 times stronger than that for the other electrode configurations, consistent with the more pronounced amnestic effects of BL ECT; and (3) neglecting the WM conductivity anisotropy results in E-field strength error up to 18% overall and up to 39% in specific ROIs, motivating the inclusion of the WM conductivity anisotropy in accurate head models. This computational study demonstrates how the realistic finite element head model incorporating tissue conductivity anisotropy provides quantitative insight into the biophysics of ECT, which may shed light on the differential clinical outcomes seen with various forms of ECT, and may guide the development of novel stimulation paradigms with improved risk/benefit ratio.

Introduction

Electroconvulsive therapy (ECT) is a therapeutic intervention in which electric current is applied through scalp electrodes to induce a generalized seizure in anesthetized patients (Abrams, 2002; APA, 2001). Although ECT plays a vital role in the treatment of medication-resistant psychiatric disorders, such as major depression, the use of ECT has been limited by its cognitive side effects (particularly amnesia (Sackeim et al., 2007; Squire, 1986)), by cardiac complications (Nuttall et al., 2004), by the need for general anesthesia, as well as by the high rate of relapse (Sackeim et al., 1990). Despite the introduction of various improvements of ECT technique, there is still limited knowledge of how to optimally select electrode placement (Kellner et al., 2010b) or stimulus current parameters (Peterchev et al., 2010) for maximal efficacy and tolerability. Indeed, the therapeutic action and adverse side effects of ECT are highly dependent upon electrode placement and stimulus current parameters, but a complete mechanistic explanation for these relationships is still lacking. For instance, right unilateral (RUL) ECT leads to fewer cognitive side effects than bilateral frontotemporal (BL) ECT (Sackeim et al., 2000), but it is not known whether this is by virtue of lower electric field (E-field) strength in hippocampus and other regions crucial for memory. Furthermore, alternative ECT electrode configurations such as bifrontal (BF) (Abrams, 2002) and focal electrically administered seizure therapy (FEAST) (Sackeim, 2004) have been proposed with the goal of preferentially targeting frontal brain regions to reduce memory impairment, but the frontal E-field strength relative to the rest of the brain and relative to other electrode placements has not been quantified.

* Correspoinding author at: Department of Phychiatry and Behavioral Sciences, Duke University, Box 3950 DUMC, Durham, NC 27710, USA. Fax: +1 919 681 9962.
E-mail address: angel.peterchev@duke.edu (A.V. Peterchev).

1053-8119/$ – see front matter © 2011 Elsevier Inc. All rights reserved.
doi:10.1016/j.neuroimage.2011.10.029

To understand the underlying biophysical mechanisms of ECT, a few early studies undertook measurements of the E-field generated by ECT in human cadavers (Lorimer et al., 1949; Smitt and Wegener, 1944) and in an electrolytic tank containing a human half-skull (Rush and Driscoll, 1968). However, the electrolytic tank measurements did not account for the geometry and conductivity properties of the scalp and the brain. The intracerebral cadaver measurements were carried out after an uncontrolled interval of time following death, potentially resulting in altered conductivity profile of the head tissues, and the tissues were damaged in the process of inserting the recording probes, potentially altering the paths of current flow generated by the scalp electrodes. Furthermore, neither of the studies produced a high-resolution map of the E-field or the current density distributions in the brain.

In order to provide more detailed field maps, a number of computational studies have simulated the distribution of the E-field or the current density field (which equals the product of E-field and conductivity) in the brain using a volume conductor model of the head. The representation of the head in computational ECT models ranges in detail from concentric spheres (Deng et al., 2009, 2011; Weaver et al., 1976) to low-resolution realistically-shaped representations (Bai et al., 2011; Sekino and Ueno, 2002, 2004) to high-resolution anatomically-accurate models (Nadeem et al., 2003; Szmurło et al., 2006). Furthermore, a substantial number of E-field/current density modeling studies have been published in the context of other transcranial electric stimulation paradigms, again ranging from simplified to realistic head representations (Datta et al., 2008, 2009; Grandori and Rossini, 1988; Holdefer et al., 2006; Im et al., 2008; Lee et al., 2009b; Miranda et al., 2006, 2007; Nathan et al., 1993; Oostendorp et al., 2008; Parazzini et al., 2011; Rush and Driscoll, 1968; Sadleir et al., 2010; Salvador et al., 2010; Saypol et al., 1991; Stecker, 2005; Suh et al., 2009, 2010; Suihko, 2002; Wagner et al., 2007). However, these studies have various limitations. The spherical and simplified geometry models do not fully account for tissue inhomogeneity and anisotropy, and the complex geometries of head tissues, including orifices in the skull such as the auditory canals and the orbits. The published anatomically-accurate ECT models (Nadeem et al., 2003; Szmurło et al., 2006) consider only isotropic tissue conductivity, explore only a limited set of electrode configurations (BL and RUL), and do not perform region of interest (ROI) analysis of the field distribution in the brain. The computational models of non-ECT transcranial electric stimulation offer some insights into the biophysics of the problem, but do not provide data specific to ECT electrode configurations and stimulus current parameters.

For realistic models of the E-field generated by ECT, the inclusion of anisotropic conductivity of the white matter (WM) may be of particular importance since the E-field induced by ECT is typically widespread and reaches deep brain regions (Deng et al., 2011; Nadeem et al., 2003), and since depression itself is associated with regionally specific abnormalities of the WM fractional anisotropy (Korgaonkar et al., 2011; Wu et al., 2011). Our and other groups have previously incorporated tissue anisotropic conductivity in models of electroencephalography and magnetoencephalography (Gullmar et al., 2006, 2010; Hallez et al., 2008, 2009; Haueisen et al., 2002; Kim et al., 2003; Lee et al., 2008, 2009a; Marin et al., 1998; Rullmann et al., 2009; Wolters et al., 2006), transcranial direct current stimulation (tDCS) (Lee et al., 2009b; Oostendorp et al., 2008; Suh et al., 2009, 2010), deep brain stimulation (Butson et al., 2007), transcranial magnetic stimulation (TMS) (De Lucia et al., 2007; Thielscher et al., 2011), and electrical impedance tomography (Abascal et al., 2008). These studies demonstrate that anisotropic conductivity of the brain tissue can have a non-negligible effect on the electromagnetic field solutions. However, computational models of ECT have not incorporated tissue conductivity anisotropy to date.

No direct and non-invasive in vivo measurement of brain conductivity anisotropy is available, but the similarity between the transportation processes of electrical charge carriers and water molecules enables estimation of the effective electrical conductivity tensors from the water self-diffusion tensors which can be non-invasively acquired with diffusion tensor magnetic resonance imaging (DT-MRI) (Basser et al., 1994b). Several methods have been proposed to derive the WM anisotropic conductivity from the measured diffusion tensors. In the effective medium approach (Tuch et al., 1999, 2001), the WM anisotropic conductivity tensors were directly calculated by a linear scaling of the diffusion tensors using an empirically determined scaling factor (Haueisen et al., 2002; Tuch et al., 1999, 2001). However, Rullmann et al. (2009) and Gullmar et al. (2010) have pointed out that using this linear scaling approach may lead to extremely large anisotropic ratios in the resulting conductivity tensors. An alternative is the volume constraint approach where the WM anisotropic conductivity tensors are computed with a fixed anisotropic ratio in each WM voxel, under the assumption that the shape of the WM diffusion tensors is prolate (cigar-shaped), rotationally symmetric ellipsoid (Shimony et al., 1999; Wolters et al., 2006). With this method, the fixed anisotropic conductivity ratio of the WM tissue can be obtained from direct measurements, e.g., 10:1 for parallel:normal orientation relative to the nerve fibers (Nicholson, 1965). Another anisotropy modeling technique is based on the linear conductivity-to-diffusivity relationship in combination with a constraint on the magnitude of the electrical conductivity tensor (Hallez et al., 2008, 2009). A "volume fraction algorithm" considering the partial volume effects of the cerebrospinal fluid (CSF) and the intravoxel fiber crossing structure has also been suggested (Wang et al., 2008), but no further studies using this approach have been reported.

In summary, existing studies of the E-field or current density resulting from ECT have investigated few electrode configurations in realistic-geometry head models, have not incorporated tissue conductivity anisotropy, and have not carried out analysis of the E-field strength in specific brain ROIs. Addressing these limitations, in the present study we develop an anatomically-accurate finite element (FE) model of the human head incorporating tissue heterogeneity and WM anisotropic conductivity, based on individual structural MRI and DT-MRI scans. We use the head model to simulate the E-field generated in the brain by the BL, BF, RUL, and FEAST ECT electrode configurations. We quantify the differences in E-field strength among the various ECT electrode configurations in brain ROIs that have putative role in the therapeutic action and/or adverse side effects of ECT. This analysis enables us, for example, to explore whether forms of ECT associated with fewer cognitive side effects induce lower E-field strengths in hippocampus, and to evaluate the degree to which frontal electrode configurations (BF and FEAST) achieve focal frontal stimulation. We also investigate how the WM conductivity anisotropy affects the E-field distribution in the brain. This study demonstrates the utility of anatomically-realistic computational models to provide clinically salient analysis and recommendations for the optimization of ECT. Preliminary results from this study were previously presented in part in conference proceedings (Lee et al., 2010, 2011).

Materials and methods

The steps of the E-field modeling and analysis are diagrammed in Fig. 1 and described below.

MRI and DT-MRI data acquisition and preprocessing

To construct an individual volume conductor model of the head, T1-weighted MRI and diffusion weighted MRI data sets of a healthy subject (28 year old male) were acquired with a 3 T MRI scanner (Magnum 3.0, Medinus Inc., Republic of Korea). The MRI images captured the head above the level of the auditory canal, including the complete brain (see Figs. 2(a) and 3(top row)). The T1-weighted structural MRI data were obtained using a standard anatomical MR imaging sequence (TR = 35 ms; TE = 7 ms; 180 slices; $1 \times 1 \times 1$ mm^3 voxel; FOV = 256 mm). The diffusion weighted MRI data were

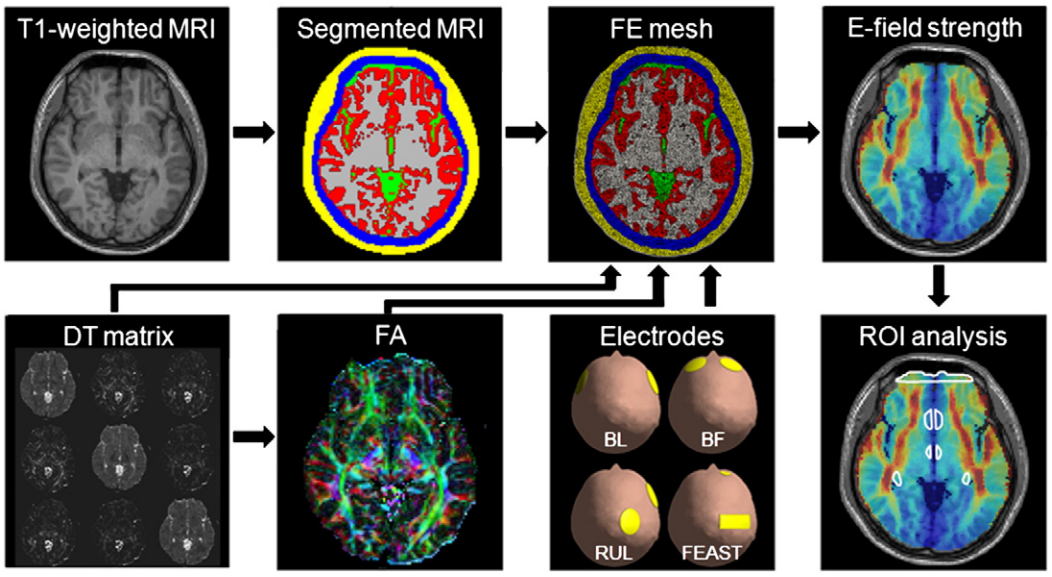

Fig. 1. Schematic illustration of the methods for generating a realistic finite element (FE) head model incorporating white matter (WM) anisotropic conductivity for E-field simulation and region of interest (ROI) analysis of ECT. T1-weighted MRI and diffusion-weighted MRI data sets of the subject are acquired. The T1-weighted MRI images are segmented into five tissues: scalp (yellow), skull (blue), cerebrospinal fluid (CSF, green), gray matter (red), and WM (gray). A diffusion tensor (DT) matrix and a fractional anisotropy (FA) map are computed from the diffusion-weighted MRI data. The color-coded FA map represents the principal orientations (largest eigenvectors) of the tensors (red: left-right, green: anterior–posterior, and blue: superior–inferior). ECT electrode representations—bilateral frontotemporal (BL), bifrontal (BF), right unilateral (RUL), or focal electrically administered seizure therapy (FEAST)—are added to the head model. The complete 3D ECT models are discretized into FE meshes, and the E-field distribution is calculated using the FE method. The E-field is then analyzed both globally and in specific brain ROIs. ROI outlines in white from top to bottom show frontal pole, subcallosal cingulate cortex (SCC), hypothalamus, and hippocampus.

acquired using a single-shot spin-echo echo-planar imaging sequence (TR = 8280 ms; TE = 70 ms; 70 contiguous slices; $1.75 \times 1.75 \times 2$ mm^3 voxel; 2 averages). The diffusion sensitizing gradients with a b-value of 600 s/mm^2 were applied in 45 non-collinear directions. The diffusion weighted images were corrected to remove eddy current and subject motion artifacts. We then computed the diffusion tensor for each voxel of the DT-MRI data set based upon a mono-exponential relationship between the signal attenuation and the diffusion tensor matrix (Basser et al., 1994a). We also extracted the region corresponding to the subject's head from the background noise and artifacts in the T1-weighted MRI data set by applying a morphological processing technique that included opening and closing of the head binary masks.

Tissue segmentation

For FE volume conductor modeling, the T1-weighted MRI was first coregistered to the DT-MRI using SPM5 (http://www.fil.ion.ucl.ac.uk/spm/) in order to avoid the transformation of the diffusion tensors (Abascal et al., 2008; De Lucia et al., 2007; Hallez et al., 2008, 2009). In this process, a voxel similarity-based registration technique was applied to acquire coregistered T1-weighted MRI by maximizing mutual information that measures the degree of mutual dependence between the image intensities of corresponding voxels in both images (Wells et al., 1996). To generate the FE meshes from the coregistered structural MRI images, the MRI images were segmented into five different sub-regions including scalp, skull, CSF, gray matter, and WM. BrainSuite2 (Shattuck and Leahy, 2002) was used to extract brain tissue compartments (gray matter and WM) as well as CSF regions including the ventricles. We then segmented the skull and scalp regions using a skull extraction algorithm (Dogdas et al., 2005) based on a combination of thresholding and mathematical morphological operations including opening and closing.

ECT electrode configurations

We added realistically-shaped ECT electrodes to the 3D head model by intersecting cylindrical or rectangular solid geometries with the head rendering. We modeled three conventional electrode placements (BL, BF, and RUL) (Abrams, 2002; APA, 2001) and an investigational configuration (FEAST) (Sackeim, 2004; Spellman et al., 2009) diagrammed in Fig. 1. Standard round electrodes (5 cm diameter) were modeled for the BL, BF, and RUL electrode configurations. For BL ECT, the two electrodes were centered bilaterally at the frontotemporal positions located 2.5 cm above the midpoint of the line connecting the external canthus and tragus (APA, 2001). For BF ECT, the electrodes were placed bilaterally 5 cm above the outer angle of the orbit on a line parallel to the sagittal plane (Abrams, 2002). For RUL ECT, one electrode was centered 2.5 cm to the right of vertex and the second electrode was placed in the homologous right frontotemporal position (APA, 2001). For FEAST, a wide rectangular electrode (2.5 cm × 6.3 cm) was placed over the right motor strip and a small circular electrode (2 cm diameter) was placed over the right eyebrow. Since the conductivity of the steel electrodes is more than five orders of magnitude higher than that of the scalp (see Section Electrical conductivity assignment), the electrode surface is effectively equipotential for any practical electrode thickness. Therefore, we did not accurately model the electrode thickness but, for simplicity, kept the outer surface of the electrodes flat, resulting in the electrode thickness between the flat outer surface and the scalp curvature varying from 5 mm to 12 mm. The electrode wires were modeled as current sources respectively sourcing and sinking current in the centers of the outer electrode surface, reflecting the wiring of conventional ECT electrode paddles, even though the high conductivity and the resulting equipotential surface of the electrodes make inconsequential the exact point of injection of current from the wires to the electrodes. Finally, we did not model the electrolyte gel applied to the ECT electrode surface, since the gel's purpose is to stabilize the impedance of the electrode–scalp interface, which is already assumed in the computational model, and since the gel is largely displaced when the electrodes are pressed against the head.

Finite element meshing

For the FE mesh generation, we utilized the Computer Geometry Algorithm Library (CGAL) (http://www.cgal.org). The mesh generator

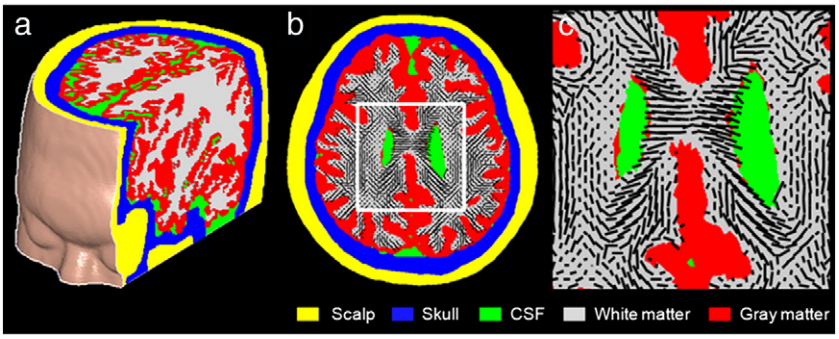

Fig. 2. (a) Partial volume rendering of the human head model. The cropped section shows the five segmented tissue compartments. (b) A transaxial conductivity map with the principal orientations (the largest eigenvectors) of the WM conductivity tensors projected as black bars onto the WM regions. (c) Enlarged view of the region framed in white in subpanel (b).

is based on the labeled voxel-volume meshing technique (Boissonnat and Oudot, 2005) and allows generation of FE tetrahedral meshes which contain one sub-mesh for each sub-domain and surface meshes that approximate the boundaries of the domain and sub-domain. The triangulation algorithm provides a discretized approximation of tissue compartments and their surface boundaries according to the restricted Delaunay triangulation paradigm (Boissonnat and Oudot, 2005; Pons et al., 2007), resulting in 3D meshes of each tissue domain and conformal surface meshes for all tissue boundaries and subdividing surfaces. The resulting FE mesh of the human head and the ECT electrodes consists of approximately 1.6 million tetrahedral elements.

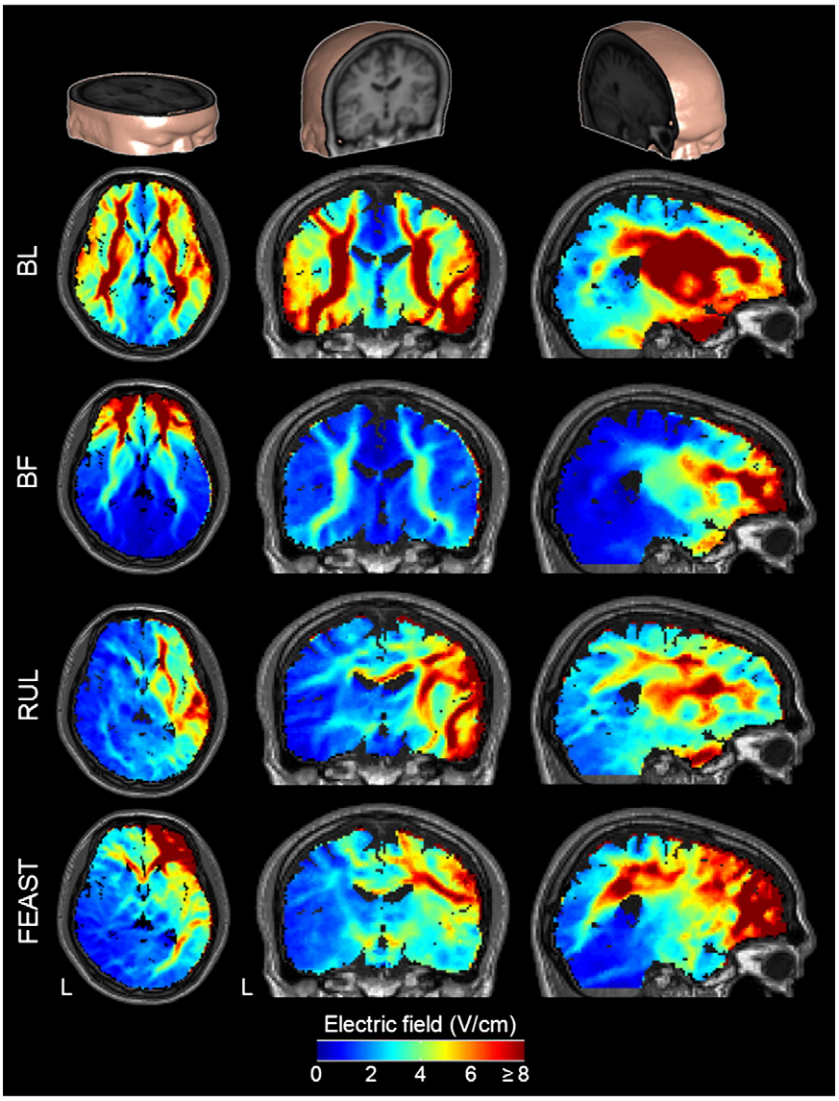

Fig. 3. Cut-away 3D rendering of the head model (top row) and the E-field magnitude spatial distribution in the anisotropic head model for BL, BF, RUL, and FEAST electrode configurations (second to bottom rows, respectively) with 800 mA current. Columns from left to right show axial, coronal, and sagittal views, respectively. The color map is clamped at an upper limit of 8 V/cm for good visibility of the electric field distribution. L: left.

Electrical conductivity assignment

To evaluate the effect of WM anisotropy on the E-field, we simulated the E-field in a model with WM anisotropic conductivity as well as in a model with fully isotropic conductivity. In the isotropic head model, the electrical conductivities were assigned to 9.8×10^5 S/m for the steel electrodes, 0.33 S/m for scalp, 0.0132 S/m for skull, 1.79 S/m for CSF, 0.33 S/m for gray matter, and 0.14 S/m (nominal) for WM (Awada et al., 1998; Kim et al., 2003; Wolters et al., 2006). In the anisotropic model, all tissues except WM were assumed to be isotropic, since the WM has the most significant anisotropic microstructure (Geddes and Baker, 1967; Nicholson, 1965). Another tissue that is often treated as anisotropic is the skull (Fuchs et al., 2007; Marin et al., 1998; Rush and Driscoll, 1968; Suh et al., 2009, 2010). However, the effective skull anisotropy originates from the macroscopic skull structure consisting of a soft (spongiform) bone layer enclosed by two hard (compact) bone layers (Akhtari et al., 2002; Fuchs et al., 2007). Therefore, the most accurate approach is to model the skull as three discrete isotropic layers (Holdefer et al., 2006; Rampersad et al., 2011; Sadleir and Argibay, 2007). In the present study, however, we modeled the skull as a single isotropic layer, since the low MRI signal from bone makes accurate skull layer segmentation difficult (Chen and Mogul, 2009), and since the mostly radial flow of current in the skull justifies the compound three-layer conductivity to be approximated by an effective radial conductivity value (Rampersad et al., 2011).

To estimate the WM anisotropic conductivity tensors, we used the assumption that the conductivity tensors share eigenvectors with the measured diffusion tensors (Basser et al., 1994b). We deployed the volume constraint approach to estimate the WM anisotropic conductivity with a fixed anisotropy ratio in each WM voxel (Wolters et al., 2006). The WM anisotropic conductivity tensor σ_{WM} was modeled to be prolate

$$\sigma_{WM} = \mathbf{S}\,\mathrm{diag}\left(\sigma_{long}, \sigma_{trans}, \sigma_{trans}\right)\mathbf{S}^{-1} \tag{1}$$

where $\mathbf{S}$ denotes the orthogonal matrix of unit length eigenvectors of the measured DTs at the barycenter of the WM tetrahedral elements. Parameters σ_{long} and σ_{trans} are the conductivity eigenvalues longitudinal (parallel) and transverse (perpendicular) to the WM fiber direction, respectively, with $\sigma_{long}\geq\sigma_{trans}$. We computed σ_{long} and σ_{trans} from the WM isotropic conductivity value of $\sigma_{iso}=0.14$ S/m and the anisotropic factor k (Gullmar et al., 2010; Wolters et al., 2006)

$$\sigma_{long} = \sigma_{iso}k^{2/3} \tag{2}$$

$$\sigma_{trans} = \sigma_{iso}k^{-1/3}. \tag{3}$$

In the present study, we used a fixed anisotropy ratio of 10:1 ($k=10$) (Nicholson, 1965), yielding $\sigma_{long}=0.65$ S/m and $\sigma_{trans}=0.065$ S/m.

To investigate how well isotropic models approximate the anisotropic model, we also simulated models with isotropic WM conductivity ranging from the transverse (low) conductivity estimate, $\sigma_{iso}=0.065$ S/m, to the longitudinal (high) conductivity estimate, $\sigma_{iso}=0.65$ S/m, including the nominal volume-constraint value of $\sigma_{iso}=0.14$ S/m.

E-field computation

The E-field distribution was computed with the FE method software ANSYS (ANSYS Inc., PA, USA). For all electrode configurations the current was set to 800 mA, corresponding to the conventional setting used with the MECTA Spectrum 5000Q ECT device (MECTA Corp., OR, USA). Since the current waveform frequencies in ECT are relatively low (<10 kHz), the E-field was obtained by solving the quasi-static Laplace equation with no internal sources (Bossetti et al., 2008; Plonsey and Heppner, 1967; Rattay, 1988)

$$\nabla\cdot(\sigma\nabla\Phi) = 0 \tag{4}$$

where Φ and σ are the electrical potential and the tissue conductivity tensor, respectively. The Neumann boundary conditions apply on the surface of the model

$$(\sigma\nabla\Phi)\cdot\hat{n} = 0 \tag{5}$$

where $\hat{n}$ is the unit vector normal to the outer surface of the model, except at the outer centers of the electrodes where current is injected. For each of the electrode configurations, the system of linear equations of the FE method was solved using the preconditioned conjugate gradient solver with a relative tolerance of 10^{-8}. Finally, the E-field distribution was computed by taking the gradient of the scalar potential Φ.

E-field analysis

The E-field was sampled in specific brain ROIs thought to be associated with therapeutic action of ECT, including frontal pole, orbitofrontal cortex (OFC), dorsolateral prefrontal cortex (DLPFC), thalamus, hypothalamus, and subcallosal cingulate cortex (SCC) (Abrams, 2002; Abrams and Taylor, 1976; Krystal and Weiner, 1994; Krystal et al., 1993; Mayberg, 2009; Mayberg et al., 2005; Sackeim, 2004), or with side effects of ECT, including hippocampus and insula (Kellner et al., 2010a; Lisanby et al., 2000; Sackeim et al., 2008; Squire et al., 1981). We also examined the E-field in primary motor cortex (specifically, the first dorsal interosseous (FDI) motor area) and brainstem, which are thought to be relevant to seizure initiation and motor manifestations of the seizure, respectively (Blumenfeld et al., 2003; Sackeim and Mukherjee, 1986). These ten anatomically defined ROIs were manually segmented from coronal MRI sections, based on human brain atlases and definitions in the literature (Goldstein et al., 2007; John et al., 2007; Makris et al., 1999; McCormick et al., 2006; Nakamura et al., 2008; Ranta et al., 2009; Weiss et al., 2005; Wible et al., 1997), and were verified with the BrainParser software (Tu et al., 2008). We then computed descriptive statistics of the E-field strength (median, 25th and 75th percentiles, and minimum and maximum) in each of these ROIs as well as in the whole left and right hemispheres for the BL, BF, RUL, and FEAST electrode configurations.

We assessed the effect of the WM anisotropic conductivity on the induced E-field qualitatively by plotting maps of the E-field magnitude and current density vectors, and quantitatively by calculating the relative difference in E-field magnitude between the two solutions in various ROIs. The difference between the isotropic and anisotropic solutions was quantified by the statistical measure of relative error, defined as

$$\text{Relative Error} = \sqrt{\frac{\sum_{i=1}^{n}\left(E_i^{iso}-E_i^{aniso}\right)^2}{\sum_{i=1}^{n}\left(E_i^{aniso}\right)^2}} \tag{6}$$

where n is the number of samples in the respective ROI, and E^{iso} and E^{aniso} denote the E-field magnitude in the isotropic and anisotropic models, respectively (Drechsler et al., 2009; Kim et al., 2003; Klepfer et al., 1997; Lee et al., 2006, 2009b).

Results

3D finite element head model

The human head model used for the E-field simulation is displayed in Fig. 2. Fig. 2(a) shows a cut-away 3D rendering of the head model. The cropped section illustrates the five segmented tissue types using the color convention defined in Fig. 1. Fig. 2(b) shows a transaxial conductivity map with the principal orientation of the electrical conductivity tensors (corresponding to the orientation of the WM fibers) projected as black bars onto the WM regions. For clarity, a portion of the conductivity map framed in white in Fig. 2(b) is magnified in Fig. 2(c).

Comparison of ECT electrode configurations

Fig. 3 shows a set of results for the spatial E-field magnitude distribution in the head model incorporating a fixed WM anisotropy ratio of 10:1. A qualitative comparison of the spatial E-field distributions in Fig. 3 indicates that the different ECT electrode configurations

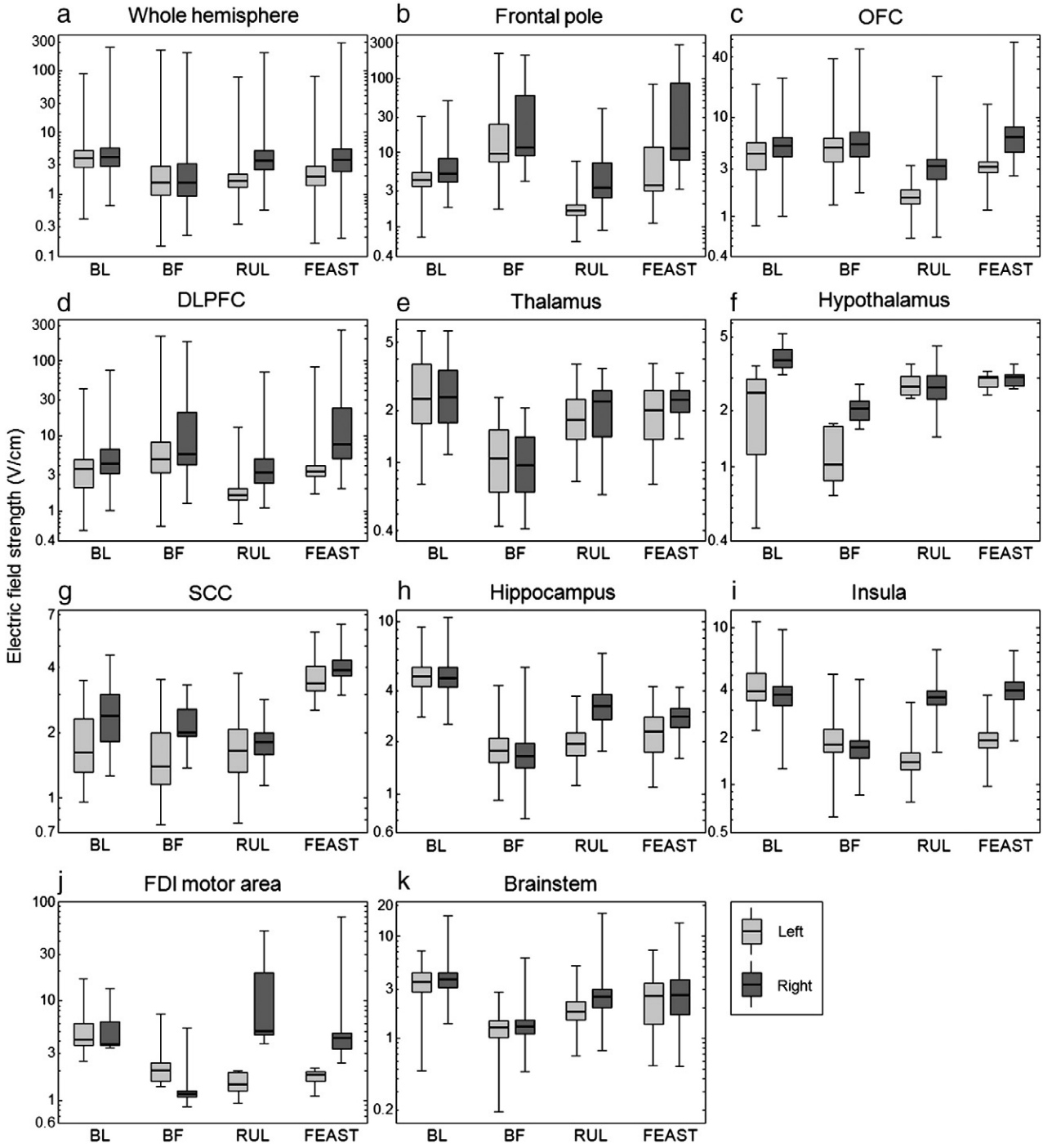

Fig. 4. Descriptive statistics of the regional E-field magnitude generated by the four ECT electrode configurations in the left and right hemispheres of the anisotropic head model. The E-field strength (y-axis) is shown on a logarithmic scale. The boxes indicate the interquartile range (25th to 75th percentile) with the median marked by a thick horizontal black line. The whiskers delimit the minimum and maximum of the regional E-field distribution.

result in distinct E-field distributions in the brain. As expected, the strongest E-field tends to occur in the brain volume under and between the two electrodes, although the detailed distribution is complex and depends heavily on the head anatomy. The symmetric ECT electrode configurations (BL and BF) have comparable E-field strength in both hemispheres, whereas the lateralized configurations (RUL and FEAST) generate higher E-field magnitude in the right hemisphere. Similarly, configurations with anterior electrodes (BF and FEAST) induce stronger E-fields in the anterior portions of the brain than the other configurations with more posterior electrodes (BL and RUL).

Fig. 4 shows descriptive statistics of the E-field strength (median, 25th and 75th percentiles, and minimum and maximum) in various ROIs in the left and right hemispheres of the anisotropic head model for each ECT electrode configuration. The median E-field strength in the whole brain is 3.9, 1.5, 2.3, and 2.6 V/cm, and the right-to-left hemisphere median E-field ratio is 1.0, 1.0, 2.1, and 1.9 for the BL, BF, RUL, and FEAST configurations, respectively. Besides generating the strongest E-field overall, BL ECT produces the highest median E-field in the hippocampi (4.8 V/cm), which is 1.5–2.8 times stronger than the hippocampal E-field of the other electrode configurations. In comparison to BL, RUL ECT has weaker median E-fields in all regions except in the right FDI motor area, where it is 1.4 times stronger. The ratio of the frontal (frontal pole, OFC, and DLPFC) to temporal (hippocampus) median E-field is 0.9, 3.5, 0.9, and 1.7 for the BL, BF, RUL, and FEAST configurations, respectively. Due to its frontal electrode placement, BF ECT has the highest frontal-to-temporal field ratio (3.5) among the configurations, inducing the strongest E-field in the frontal pole as well as substantial field strength in the OFC and DLPFC. Compared to the BF and RUL electrode placements, FEAST produces stronger median E-field stimulation in thalamus, hypothalamus, SCC, and insula. Moreover, compared to all of the other configurations, FEAST induces 1.2–2.0, 1.4–2.4, and 1.6–2.2 times stronger E-fields in the right OFC, DLPFC, and SCC, respectively.

Effect of white matter anisotropic conductivity

To demonstrate the effect of WM anisotropy on the E-field and current density solutions, in Fig. 5 we plotted maps of the E-field magnitude and the current density vector field in a coronal slice (same as in Fig. 3 (middle column)) for BL and RUL ECT in the nominal isotropic (WM $\sigma_{iso} = 0.14$ S/m) and anisotropic head models. In this slice, the BL and RUL configurations generate, respectively, predominantly mediolateral and inferosuperior current flow. In both the isotropic and anisotropic models, the high conductivity of CSF-filled structures tends to channel current flow, as illustrated by the

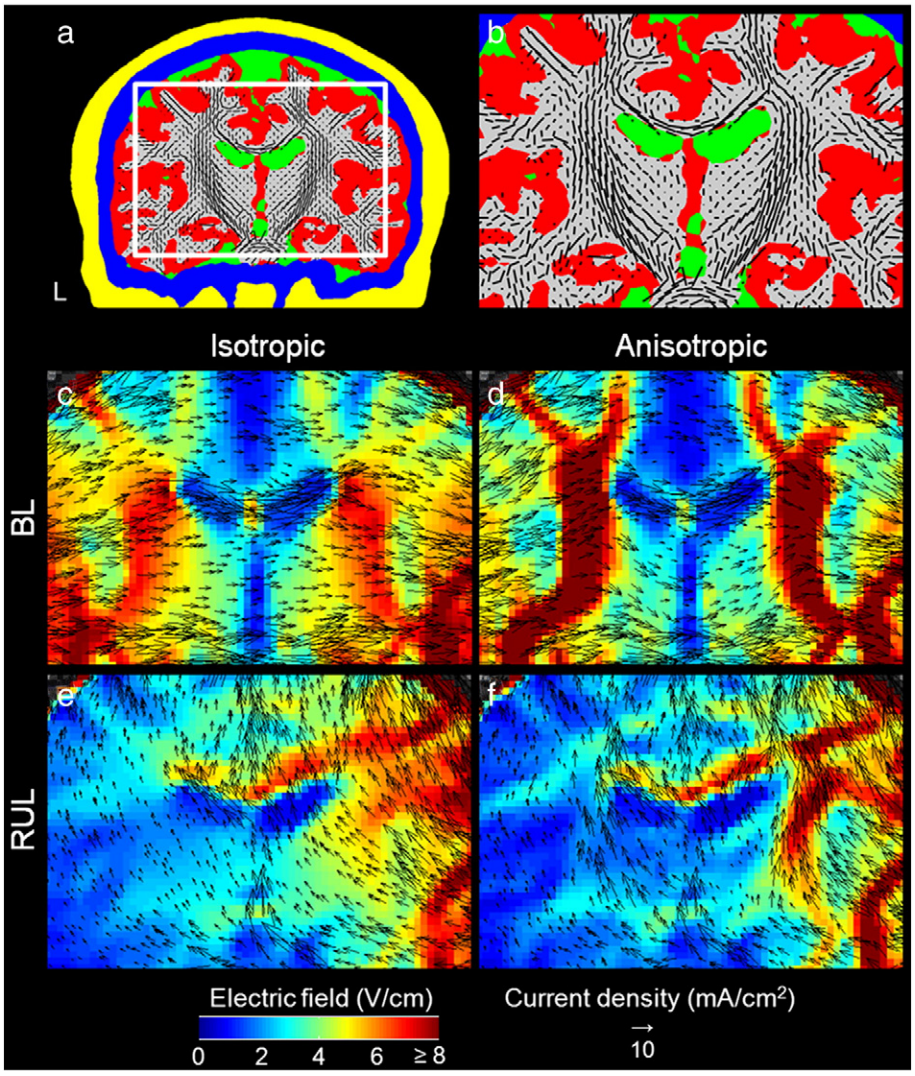

Fig. 5. Comparison of the isotropic and anisotropic model simulations. (a) A coronal slice conductivity map using the same display conventions as in Fig. 2. (b) Enlarged view of the region framed in white in (a). (c–f) View corresponding to (b) of the E-field magnitude distribution (in color scale) and current density vector field of the isotropic (left) and anisotropic (right) head models for BL (middle row) and RUL (bottom row) electrode configurations. L: left.

larger arrows in the lateral ventricles in Figs. 5(c) and (d) and in the longitudinal fissure in Figs. 5(e) and (f). Despite the higher current density in CSF-filled structures, the E-field magnitude there is relatively low (blue color) due to the high conductivity. Compared to the isotropic models (Figs. 5(c) and (e)), in the anisotropic models (Figs. 5(d) and (f)) additional channeling effects emerge as a result of the WM fiber orientation. For example, when the current flow is partially aligned with the orientation of the WM fibers, the anisotropic model enhances the current alignment with the fibers, as demonstrated by the curving of the current flow along the WM fibers in the corpus callosum and in the regions inferior to the lateral ventricles in BL ECT (Figs. 5(d) versus (c)). Furthermore, long stretches of fibers aligned with the current flow can result in denser current along the fibers, as demonstrated by the concentrated current flow along the inferosuperior-oriented internal capsule fibers in both hemispheres in RUL ECT (Figs. 5(f) versus (e)). On the other hand, current flowing in direction transverse to the WM fiber orientation generates a relatively high E-field magnitude due to the lower electrical conductivity across the WM fibers, as exemplified by the regions well demarcated in red color in the BL E-field map (Figs. 5(d) versus

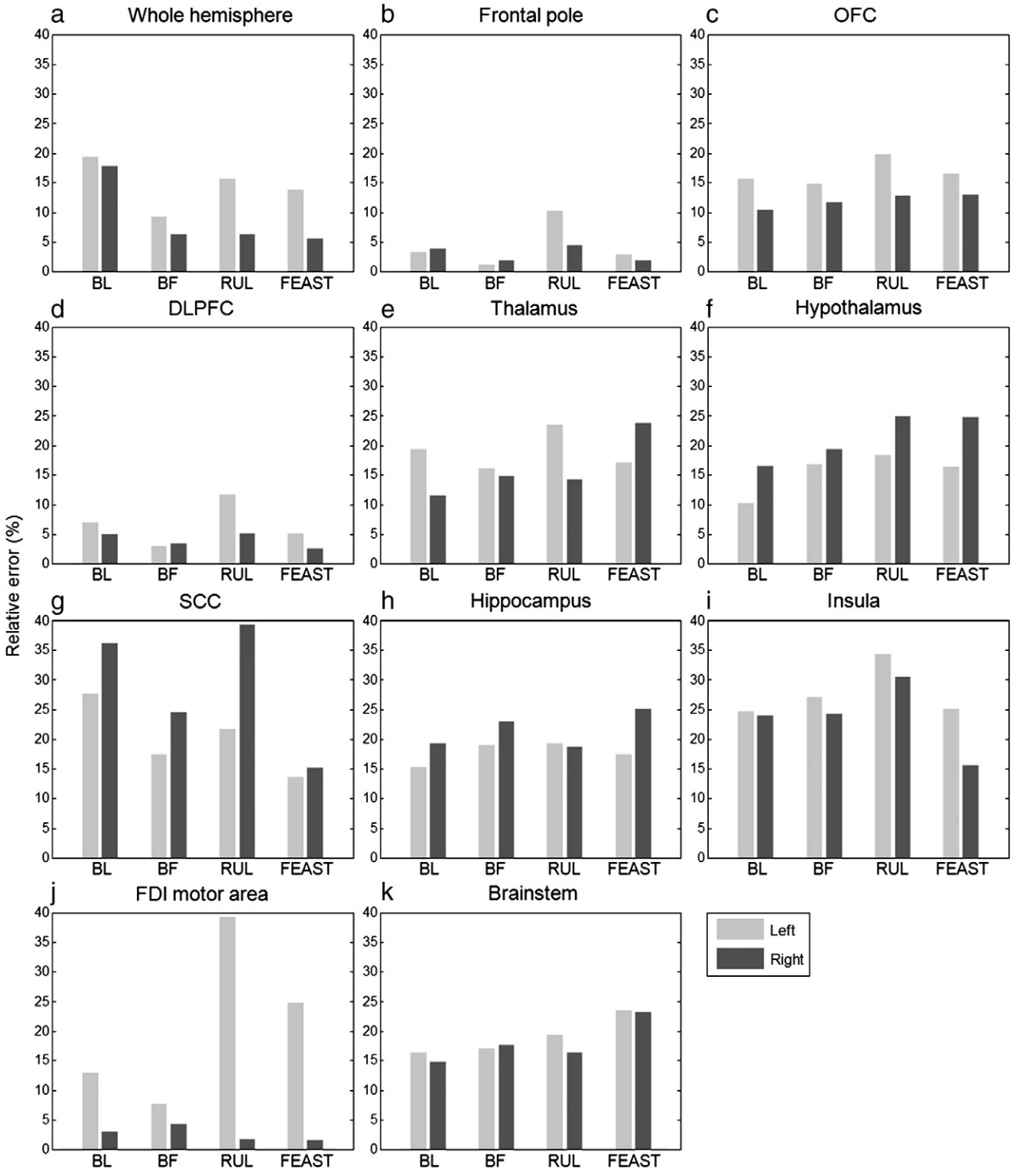

Fig. 6. Relative error of the E-field magnitude in the isotropic versus the anisotropic head model for the various brain ROIs and ECT electrode configurations. Relative error is defined in Eq. (6).

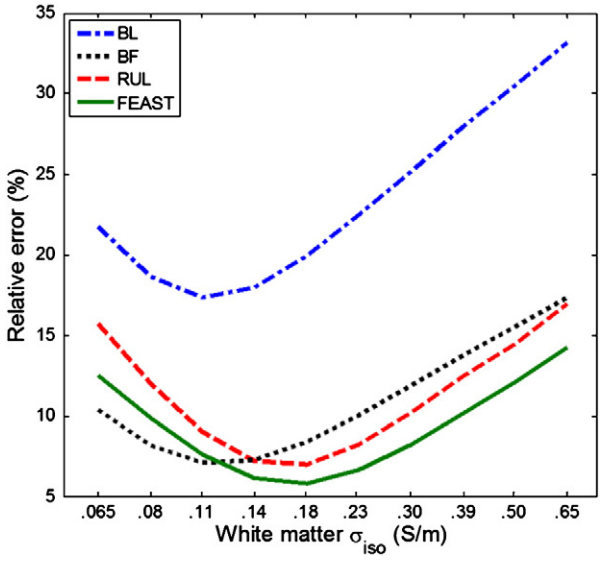

Fig. 7. E-field magnitude relative error in the whole brain between the anisotropic head model (WM $\sigma_{long} = 0.65$ S/m and $\sigma_{trans} = 0.065$ S/m) and the isotropic model with WM conductivity ranging from $\sigma_{iso} = 0.065$ S/m to 0.65 S/m. The four curves correspond to the four ECT electrode configurations.

(c)) corresponding to lateromedial current flow across inferosuperior and anteroposterior oriented pyramidal tract fibers.

Quantitatively, the E-field magnitude relative error over the whole brain of the nominal isotropic model (WM $\sigma_{iso} = 0.14$ S/m) compared to the anisotropic model is 18%, 7%, 7%, and 6% for BL, BF, RUL, and FEAST ECT, respectively. Fig. 6 breaks these data down for distinct ROIs in the left and right hemispheres. The largest ROI error (39%) is observed in the left FDI motor area for RUL ECT, and the lowest error (1%) occurs in the left frontal pole for BL ECT. In prefrontal and frontal areas including frontal pole, OFC, and DLPFC in Figs. 6 (b)–(d), the maximal error of 19% occurs with RUL ECT in the left OFC. The SCC in Fig. 6(g) exhibits relatively larger differences compared to other ROIs, ranging from 14% (FEAST) to 39% (RUL). In hippocampus and insula, the largest errors are 25% and 34%, respectively.

Fig. 7 shows the relative error in E-field magnitude over the whole brain between the isotropic and anisotropic models as a function of the WM conductivity in the isotropic model. The largest errors occur with the highest isotropic conductivity of 0.65 S/m for all configurations. The lowest errors, indicating the "best" isotropic model match to the anisotropic model, are at $\sigma_{iso} = 0.11$ S/m for BL and BF ECT and at $\sigma_{iso} = 0.18$ S/m for RUL and FEAST ECT, which are close to but distinct from the volume-constraint value of $\sigma_{iso} = 0.14$ S/m.

Discussion and conclusions

Even though the E-field spatial distribution is a key aspect of dosage in ECT, it has not been accurately characterized. The spatial distribution of the E-field strength is a determinant of which brain regions are directly activated by the electric stimulation delivered by various ECT electrode configurations. This work represents the first quantitative study investigating the regional differences in E-field strength resulting from variations in the ECT electrode configuration in an anatomically realistic head model.

Implications for ECT technique

It has been suggested that the flow of electric current and a resultant robust seizure expression in the prefrontal cortex is requisite to the antidepressant effects of ECT, as demonstrated, for example, by the superior efficacy of BL ECT compared to low dose RUL ECT (Abrams and Taylor, 1976; Ottosson, 1960; Sackeim, 2004). This view has motivated electrode configurations designed to target the prefrontal cortex, such as BF and FEAST. The results from our model confirm that BL ECT generates stronger E-field in anterior portions of the brain compared to RUL ECT. Our results further indicate that BF and FEAST generally produce higher E-field strengths in prefrontal structures compared to BL and RUL ECT (see Figs. 3 and 4). In particular, compared to the other electrode configurations, BF produces the highest E-field magnitude in the frontal poles. Furthermore, FEAST produces the strongest E-field in the right OFC, DLPFC, and SCC—likely a consequence of current flow through the orbits which represent low impedance paths into the brain. Significantly, DLPFC and SCC are targets for other forms of brain stimulation with reported antidepressant efficacy. The right DLPFC has been targeted with low-frequency (inhibitory) repetitive TMS for the treatment of depression (Fitzgerald and Daskalakis, 2011). There is evidence that focal stimulation of the SCC via deep brain stimulation reduces elevated SCC activity and normalizes aberrant network activity in depression, with resultant antidepressant effect (Mayberg et al., 2005; McNeely et al., 2008). The frontal pole and OFC have strong anatomical and functional connectivity with the SCC and the rest of the dysfunctional brain network associated with depression (Gutman et al., 2009; Johansen-Berg et al., 2008; Mayberg, 2009; Mayberg et al., 2005) and therefore are potential targets for stimulation as well.

Another prevailing hypothesis on the mechanism of action of ECT focuses on diencephalic stimulation. This hypothesis states that for optimal antidepressant efficacy, the seizure must be sufficiently generalized to involve diencephalon centers, particularly the thalamus and hypothalamus (Abrams, 2002; Abrams and Taylor, 1976). Cortical–thalamocortical interactions are crucial for the initiation, propagation, and behavioral manifestations of generalized seizures (Guillery and Sherman, 2002; McNally and Blumenfeld, 2004). Thalamic processes that inhibit cortical function have been hypothesized to play a role in the antidepressant effect of ECT (Krystal and Weiner, 1994; Krystal et al., 1993; McNally and Blumenfeld, 2004; Sackeim et al., 1991). Our results show that BL ECT produces stronger E-field in the thalamus and hypothalamus compared to BF and RUL ECT, consistent with the superior antidepressant efficacy of BL ECT as compared with low dose RUL ECT, but does not explain how adequately-dosed RUL ECT matches the efficacy of BL ECT. Notably, FEAST produces E-field strengths in the diencephalon centers that are higher than in BF and RUL, and approach those in BL. However, whether this confers high antidepressant efficacy to FEAST is unknown since FEAST clinical data has not been reported.

It has been suggested that retrograde amnesia may be related to seizure activity in the medial temporal lobe (Lisanby et al., 2000; Luber et al., 2000; Squire, 1986) and consequently it was proposed that techniques inducing seizures with reduced current spread to this area may cause less memory side effects (Sackeim, 2004). The medial temporal structure specifically associated with amnesia is the hippocampus, which has been shown to be uniquely affected by induced seizures, and to have a low seizure threshold (Lisanby et al., 2000). Of all configurations in our model, BL ECT produces the strongest E-field in the hippocampi, consistent with its greater acute cognitive impairment (Kellner et al., 2010a; Sackeim et al., 2008) and short- and long-term retrograde amnesia (Lisanby et al., 2000; Squire et al., 1981) compared to BF and RUL ECT. Our results may be particularly useful for predicting the clinical effects of ECT paradigms for which clinical data is not yet available, such as FEAST. For example, the E-field strength generated by FEAST is lower than RUL in the right hippocampus, but is higher than RUL in the left hippocampus, and is higher compared to BF in both hippocampi. Therefore, one might predict that FEAST may have memory side effects lower than in BL but higher than in BF (assuming identical current levels in all configurations); this is yet to be tested clinically.

The E-field model could also inform the mechanisms behind cardiac effects of ECT. Accumulating evidence indicates that cardiovascular

regulation receives significant input from cortical structures, especially the insula (Oppenheimer, 2006). Direct electrical stimulation of the left caudal anterior insula leads to increased occurrence of bradycardia and depressor responses as a result of parasympathetic activation, whereas right anterior insular stimulation leads to tachycardia and diastolic blood pressure elevation as a result of sympathetic activation (Oppenheimer, 2006; Oppenheimer et al., 1992). Data from patients with insular lesions are consistent with left insular cardioinhibitory representation and right insular cardioexcitatory representation (Oppenheimer, 2006). During the stimulus delivery phase of ECT, a higher likelihood of heart rate reduction and longer duration of asystole were observed with RUL compared to BL and BF ECT (Nagler, 2010). Since RUL ECT produces nearly three times higher E-field strength in the right insula compared to the left insula (Fig. 4(i)), we hypothesize that the right insula is preferentially inhibited during stimulation compared to the left insula, resulting in sympathetic withdrawal. In contrast, BL and BF ECT induce similar E-field strengths in left and right insula, thus the sympathovagal balance is less affected, consistent with the lower rates of asystole observed clinically (Loo et al., 2009; Nagler, 2010). Other brain regions, such as the hypothalamus and brainstem, are also known to be involved in cardiac regulation (Welch and Drop, 1989); therefore, the E-field characteristics in these regions (Figs. 4(f) and (k)) may also contribute to cardiac effects.

Our results indicate that the E-field strengths induced by RUL are exclusively weaker than in BL ECT except in the right motor strip where the E-field magnitude induced by RUL ECT is about 38% stronger compared to BL. This observation is consistent with the lower seizure threshold of RUL compared to BL ECT, since the motor strip is thought be the likely site for seizure initiation (Sackeim and Mukherjee, 1986). We also found that BL and FEAST generate higher E-field strengths compared to BF and RUL in the brainstem which mediates the motor manifestations of generalized tonic–clonic seizures (Blumenfeld et al., 2003).

The above observations illustrate how the realistic ECT E-field model can contribute to a biophysical explanation of reported clinical differences among conventional electrode placements (BL, BF, and RUL), as well as to the evaluation and optimization of investigational configurations (e.g., FEAST). For example, the realistic head model can be coupled with an optimization algorithm to select scalp electrode locations and current strengths to target specific brain structures (Dmochowski et al., 2011; Park et al., 2011). Ultimately, this work may guide the development of novel stimulation paradigms with improved risk/benefit ratio.

Influence of tissue conductivity anisotropy

The second objective of this study was to evaluate the influence of WM conductivity anisotropy on the E-field simulation. Our results, summarized in Figs. 5 and 6, indicate that neglecting WM conductivity anisotropy and using instead the volume-constraint WM isotropic conductivity value of 0.14 S/m leads to relative errors in the E-field magnitude up to 18% for the whole brain and up to 39% within the considered ROIs. The maximum relative error was found in the left FDI motor area for RUL ECT. In addition, our results indicate that the E-field differences between the isotropic and anisotropic models depend upon the specific ECT electrode configuration used. For example, ignoring WM anisotropy produces errors in the FDI motor area E-field up to only 8% for the BF configuration, but up to 39% for the RUL configuration. Furthermore, the WM isotropic conductivity value that gives the best approximation of the anisotropic case, in terms of the lowest overall relative error, varies with electrode configuration, as shown in Fig. 7. Specifically, the optimal WM isotropic conductivity value for the lateralized configurations (0.18 S/m for RUL and FEAST) is 64% higher than that for the bilaterally symmetric configurations (0.11 S/m for BL and BF). A possible explanation for this difference is that in the lateralized electrode configurations the electrical current is more aligned, on average, with the orientation of the WM fibers than in the bilaterally symmetric configurations. The results in Fig. 7 also indicate that the volume-constraint WM isotropic conductivity (0.14 S/m) yields relative errors within 0.7% of the optima achievable with the isotropic models and is, therefore, a reasonable choice for isotropic models. Generally, the E-field magnitude errors and their sensitivity to the electrode configuration motivate the inclusion of the WM conductivity anisotropy in computational E-field models for increased accuracy.

Another important observation is that the error in the E-field strength between the isotropic and anisotropic models usually increases for brain regions that are farther away from the ECT electrodes. For example, the E-field errors in deep brain structures such as thalamus, hypothalamus, insula, and SCC (10%–39%) are higher than the errors in more superficial areas such as frontal pole and DLPFC (1%–12%) which lie closer to the scalp electrodes. Furthermore, although the overall relative error in the whole brain is higher for BL than for BF, the relative error is larger for BF than for BL in ROIs such as hypothalamus, hippocampus, insula, and brainstem that are farther away from the BF electrodes. Similarly, in the lateralized electrode configurations (RUL and FEAST), the E-field errors for highly lateralized ROIs (whole hemisphere, DLPFC, insula, and FDI motor area) are significantly larger on the left side than on the right side (where the electrodes are placed). The E-field error increase away from the electrodes could be explained in terms of the longer paths that the electrical current has to traverse from the electrodes to distant brain regions, which results in a larger cumulative error of all the differences in the conductivity tensors along the current path. Thus, incorporation of WM conductivity anisotropy in ECT E-field models is crucial for analysis of the E-field characteristics in brain regions that we try to avoid stimulating by placing the electrodes away from them. Often these are brain regions thought to be associated with adverse side effects of ECT, and thus the degree to which they are stimulated is of particular relevance to studies that evaluate ECT techniques aimed at improving safety. This observation further supports the inclusion of WM anisotropic conductivity in ECT models.

The comparison of the isotropic and anisotropic model simulations in Fig. 5 provides insight into how the orientation of WM fibers affects the current density and E-field distributions. The current flow generally follows the path of least electrical impedance. Consequently, compared to the isotropic model, current flow along the WM fibers in the anisotropic model is denser and follows the fiber orientation. In some cases the channeling of current along WM fiber tracts increases the local E-field strength, but in other cases this effect is offset by the lower impedance along the fibers, leading to reduced E-field strength. The current may steer away from segments of increased impedance resulting from the passage of WM fibers perpendicular to the current flow. However, when current comes across wide stretches of fibers perpendicular to its flow, the current cannot steer away and is forced to cross this high impedance barrier, resulting in high E-field magnitude. Thus, increased E-field strength in the anisotropic model compared to the isotropic model can result from either concentration of current flow along WM fibers that is not offset by the low impedance along the fibers, or from increased impedance for current flow perpendicular to WM fibers.

In support of our findings, other bioelectric head modeling studies have reported comparable effect sizes associated with the inclusion of WM conductivity anisotropy. We previously studied the impact of WM anisotropy on the current density distribution generated by tDCS and found relative errors of 53% and 19% in current density magnitude in the WM and gray matter, respectively (Lee et al., 2009b). Similarly, Sadleir et al. (2010) concluded that the inclusion of the WM anisotropic conductivity in a tDCS model would result in differences up to 39% in the median current density magnitude. De Lucia et al. (2007) found that WM anisotropy contributes a difference of 10% in the peak TMS-

induced E-field, which is consistent with the findings of Thielscher et al. (2011) (It should be noted that the TMS E-field is substantially more superficial than the E-field in ECT and tDCS; therefore, the lower error associated with WM anisotropic conductivity in TMS is expected). Finally, Wolters et al. (2006) reported that the inclusion of WM anisotropic conductivity results in up to 30% difference in the magnitude of electroencephalographic scalp potentials generated by dipole sources within the brain. Thus, the differences between the isotropic and anisotropic model results in these studies are comparable to the relative errors up to 39% found in our study.

It has been reported that depression itself is associated with changes in the volume of specific brain structures (Bremner, 2005; Tsopelas et al., 2011) and with regionally specific abnormalities of the WM fractional anisotropy (Korgaonkar et al., 2011; Wu et al., 2011). Patients with major depressive disorder showed a fractional anisotropy reduction up to 14% in WM, with an 8% decrease in the superior longitudinal fasciculus associated with the DLPFC (Korgaonkar et al., 2011). Neglecting WM anisotropy in our model, which is associated with fractional anisotropy reduction of 100%, results in up to 39% difference in E-field strength. Extrapolating from these data, a pathological 14% decrease in fractional anisotropy could result in approximately 6% difference in the E-field strength. Even though this effect is relatively small, tissue conductivity anisotropy and other pathological brain structure changes should be considered as a potential source of E-field variability, as their compounded effect may be significant.

Model validity and limitations

Validation of brain stimulation E-field simulations remains a challenging problem due to the unavailability of methods for high-resolution in vivo E-field measurements. Nevertheless, our results in the brain (E-field strength median of 1.5–3.9 V/cm and range of 0.1–300 V/cm) are in good agreement with published modeling and experimental measurements. In the references to other studies below, the electrode current was scaled to 800 mA to allow comparison with our data. In their anatomically-realistic computational model of BL ECT, Nadeem et al. (2003) did not report statistics on the E-field distribution, but the figures suggest a brain E-field magnitude ranging from approximately 0.1 V/cm to as high as 700 V/cm. Rescaling the current from Sadleir et al.'s (2010) and Parazzini et al.'s (2011) anatomically-realistic tDCS models and converting current density to E-field strength, the average of their reported median values is 2.5 V/cm and 2.7 V/cm, respectively. Studies using simplified model geometries or low-resolution experimental measurement techniques generally reported lower E-field strengths (Deng et al., 2011; Lorimer et al., 1949; Rush and Driscoll, 1968; Smitt and Wegener, 1944). For instance, a recent simulation study by our group of BL, BF, RUL, and FEAST ECT in a spherical head model obtained median and maximum brain E-field strength ranges of 0.6–1.2 V/cm and 2.1–2.5 V/cm, respectively (Deng et al., 2011). Rush and Driscoll's (1968) measurements of a frontal–occipital electrode configuration in a half-skull immersed in an electrolytic tank yielded maximum E-field in the range of 1.5–2.5 V/cm. Intracerebral measurements in cadaver heads with stimulation current applied through bifrontotemporal electrodes produced maximum E-field strength estimates of 0.7–1.8 V/cm (Lorimer et al., 1949; Smitt and Wegener, 1944). A likely factor contributing to the lower E-field strengths reported in these studies is the effective averaging out of the spatial distribution of the E-field resulting from the simplified head models and/or from the low-resolution spatial sampling of the electric potentials in the cadaver measurements. Indeed, a study comparing head models for TMS found a ~51% increase of the maximum E-field strength in the anatomically-realistic model compared to simplified spherical models (Thielscher et al., 2011).

A limitation of the present study that may impact the E-field strength and distribution is the truncation of the head model. The T1-weighted MRI data was only acquired for the portion of the head above the level of the auditory canal. The truncated head model eliminates shunting of the ECT stimulus current in the lower portion of the head, resulting in increased E-field magnitude in the brain. Further, the head model truncation has differential effects for various ECT electrode placements. For example, in our ECT analysis using a spherical head model (data not shown), we observed that truncation of the head model results in a 52% and 27% increase in the median E-field and a 41% and 14% increase in the peak E-field for BL and RUL ECT, respectively. Therefore, future ECT head models should be based on structural MRI and DT-MRI data set of the whole head including the skull base and a portion of the neck underneath.

Uncertainty about the thickness, structure, and conductivity of the various tissues in the model can contribute to inaccuracies of the simulated E-field and to discrepancies among various models and experimental measurements (Bikson and Datta, 2011), but it is difficult to assess the extent of these uncertainties since, as discussed in the beginning of this section, there are no adequate empirical data to compare simulations to. For example, we observed overall comparable E-field strength in the left and right hemispheres for the symmetric ECT electrode configurations (BL and BF). However, certain regions such as hypothalamus, SCC, and FDI motor area produced asymmetric results of the median E-field magnitude (see Fig. 4). This may be due to intrinsic anatomical asymmetry and/or errors in the tissue segmentation and the ROI boundary definition between the two sides of the head, but it is difficult to determine how much each of these factors is contributing.

There are two distinct sources of uncertainty that confound the conclusions of modeling studies: first, naturally occurring anatomical variability in the population and, second, errors in the tissue segmentation and tissue conductivity within the modeled individual(s). We have previously investigated the effect on the induced E-field in a spherical head model of varying the thickness and conductivity of various tissue layers within ranges reported in the literature (Deng et al., 2009). That study reported that, for example, individual male scalp and skull thickness variation, which can be as high as 58% and 34% of the average, resulted in up to 76% and 20% changes of the peak brain E-field, respectively (Deng et al., 2009). The present study does not account for anatomical variability in the population since it is based on imaging data of a single individual; this limitation has to be considered when applying these results to interpret clinical ECT data obtained from various individuals. Nevertheless, the methods presented in this paper are general and can be applied to any individual with appropriate MRI data.

The second source of uncertainty is modeling errors of the tissue structure and electrical properties within an individual model. For example, the average thickness of the scalp, skull, and CSF underlying the skull are about 5.5 mm, 7 mm, and 3 mm, respectively (Deng et al., 2009), and the T1-weighted structural MRI data used to create our model has spatial resolution of 1 mm. Therefore, the MRI resolution contributes potential error of approximately 18%, 14%, and 33% to the thickness of the scalp, skull, and CSF, corresponding to estimated errors in the peak brain E-field up to 24%, 11%, and 14%, respectively, based on our perturbation data in the spherical male head model (Deng et al., 2009). Further, even though a single skull layer is a reasonable choice for spherical models, the nonuniformity of the compact and spongiform layers in a real skull motivates the segmentation of these layers in a high-accuracy model (Rampersad et al., 2011), which may require coregistering the MRI scan with a computed tomography scan that provides substantially stronger signal from bone (Chen and Mogul, 2009). There is also a wide spread of tissue conductivity values reported in the literature, especially for the skull (Deng et al., 2009), and it is not known how much of this variability is attributable to individual variation and how much—to measurement error. For example, in this study we used skull conductivity value of 0.0132 S/m whereas other studies have used lower values,

e.g., 0.0083 S/m (Deng et al., 2011). Compared to a simulation of our realistic head model with the lower skull conductivity of 0.0083 S/m (data not shown), the nominal model with skull conductivity of 0.0132 S/m increases the median E-field magnitude in the brain by 13%, 10%, 16%, and 16% for BL, BF, RUL, and FEAST ECT, respectively. These estimates of E-field variability due to potential tissue thickness and conductivity errors are commensurate with the E-field relative errors up to 18% overall and up to 39% in specific ROIs that result from neglecting WM anisotropy in the present study. Therefore, it could be argued that accounting for WM anisotropy is as important to E-field strength estimation as accurate tissue segmentation and conductivity assignment. Beyond that, anisotropic models may give more accurate E-field directionality information, as suggested by Fig. 5, which may be particularly relevant if the E-field data were coupled with neural models which are direction sensitive (Radman et al., 2009; Rushton, 1927).

In our anisotropic volume conductor modeling, we adopted the volume constraint algorithm to estimate the WM anisotropic conductivity tensors with the assumption of a fixed anisotropy ratio of 10:1 in each WM voxel (Wolters et al., 2006). However, this approach may overestimate the actual ratio of the WM anisotropic conductivity tensors (Hallez et al., 2008). In reality, the ratio of longitudinal to transverse WM conductivity varies. For example, the fractional anisotropy map shown in Fig. 1 indicates that strong anisotropy is present in the pyramidal tracts and corpus callosum. On the other hand, cortical brain regions include lower degree of WM anisotropy, which is associated with lower anisotropic conductivity ratios. Recently, Bangera et al. (2010) conducted an experimental validation of anisotropic head models by measuring intracranial electric potentials generated by stimulation with an implanted dipole source in the human brain (Bangera et al., 2010). Two different anisotropic models using, respectively, the effective medium approach (Tuch et al., 1999, 2001) and the volume constraint approach with fixed 10:1 anisotropy ratio (Wolters et al., 2006) were compared revealing that the former results in a better fit to the experimental data than the latter. In the present study, we did not examine alternative approaches for estimating the anisotropic conductivity tensors such as the effective medium approach (Tuch et al., 1999, 2001) and its constrained version (Hallez et al., 2008, 2009). Our model allows a relatively uncomplicated incorporation of various anisotropy estimation approaches which could be investigated in future studies.

It should be also acknowledged that the present simulations address only the E-field distribution and not the direct neural activation and the resultant seizure, the topography of which is also considered to be a major contributor to clinical outcome. At present there are no computational models that can realistically simulate the induction and propagation of seizures throughout the whole brain. Because we cannot realistically simulate the neural response to ECT, we did not explore the effect of various parameters of the ECT stimulus current such as the current amplitude, pulse width, and frequency. Nevertheless, since the E-field strength is directly proportional to the stimulus current amplitude, our data can be straightforwardly scaled to other current intensities. Furthermore, systematic data on the clinical effects of various current amplitudes is presently lacking as ECT is done exclusively with fixed current amplitudes of 800 mA or 900 mA (Peterchev et al., 2010). We have previously used the assumption of a single neural activation threshold throughout the brain to explore the effect of the stimulus current amplitude on the focality of direct neural activation in a spherical head model, and have suggested that reduction and individualization of the current may be productive strategies for better targeting of ECT (Deng et al., 2010, 2011; Peterchev et al., 2010). However, more empirical data linking the E-field characteristics to seizure induction have to be accumulated to support the incorporation of neural dynamics in the realistic head model, which would, in turn, enable explanation of the effect of the stimulus current parameters.

Acknowledgment

This work was supported by the National Institutes of Health under grant R01MH091083, the National Science Foundation through TeraGrid resources provided by National Center for Supercomputing Applications under grant TG-MCB100050, and the Korea Science and Engineering Foundation (KOSEF) grant funded by the Korean government (MEST) (No. 2009-0075462). We would like to thank Drs. Richard Weiner and Andrew Krystal from the Department of Psychiatry and Behavioral Sciences at Duke University for their helpful comments and suggestions.

References

Abascal, J.F.P.J., Arridge, S.R., Atkinson, D., Horesh, R., Fabrizi, L., De Lucia, M., Horesh, L., Bayford, R.H., Holder, D.S., 2008. Use of anisotropic modelling in electrical impedance tomography: description of method and preliminary assessment of utility in imaging brain function in the adult human head. Neuroimage 43, 258–268.

Abrams, R., 2002. Electroconvulsive Therapy, 4th ed. Oxford Unversity Press, New York.

Abrams, R., Taylor, M.A., 1976. Diencephalic stimulation and the effects of ECT in endogenous depression. Br. J. Psychiatry 129, 482–485.

Akhtari, M., Bryant, H.C., Marnelak, A.N., Flynn, E.R., Heller, L., Shih, J.J., Mandelkern, M., Matlachov, A., Ranken, D.M., Best, E.D., DiMauro, M.A., Lee, R.R., Sutherling, W.W., 2002. Conductivities of three-layer live human skull. Brain Topogr. 14, 151–167.

APA, 2001. The Practice of Electroconvulsive Therapy: Recommendations for Treatment, and Privileging: A Task Force Report of the American Psychiatric Association. American Psychiatric Association, Washington.

Awada, K.A., Jackson, D.R., Baumann, S.B., Williams, J.T., Wilton, D.R., Fink, P.W., Prasky, B.R., 1998. Effect of conductivity uncertainties and modeling errors on EEG source localization using a 2D model. IEEE Trans. Biomed. Eng. 45, 1135–1145.

Bai, S., Loo, C., Abed, A.A., Dokos, S., 2011. A computational model of direct brain excitation induced by electroconvulsive therapy: comparison among three conventional electrode placements. Brain Stimul. doi.org/10.1016/j.brs.2011.07.004.

Bangera, N.B., Schomer, D.L., Dehghani, N., Ulbert, I., Cash, S., Papavasiliou, S., Eisenberg, S.R., Dale, A.M., Halgren, E., 2010. Experimental validation of the influence of white matter anisotropy on the intracranial EEG forward solution. J. Comput. Neurosci. 29, 371–387.

Basser, P.J., Mattiello, J., Lebihan, D., 1994a. Estimation of the effective self-diffusion tensor from the NMR spin-echo. J. Magn. Reson. 103, 247–254.

Basser, P.J., Mattiello, J., Lebihan, D., 1994b. MR diffusion tensor spectroscopy and imaging. Biophys. J. 66, 259–267.

Bikson, M., Datta, A., 2011. Guidelines for precise and accurate computational models of tDCS. Brain Stimul. http://dx.doi.org/10.1016/j.brs.2011.06.001.

Blumenfeld, H., Westerveld, M., Ostroff, R.B., Vanderhill, S.D., Freeman, J., Necochea, A., Uranga, P., Tanhehco, T., Smith, A., Seibyl, J.P., Stokking, R., Studholme, C., Spencer, S.S., Zubal, I.G., 2003. Selective frontal, parietal, and temporal networks in generalized seizures. Neuroimage 19, 1556–1566.

Boissonnat, J.D., Oudot, S., 2005. Provably good sampling and meshing of surfaces. Graph. Model. 67, 405–451.

Bossetti, C.A., Birdno, M.J., Grill, W.M., 2008. Analysis of the quasi-static approximation for calculating potentials generated by neural stimulation. J. Neural Eng. 5, 44–53.

Bremner, J.D., 2005. Changes in brain volume in major depression. Depress. Mind Brain 2, 38–46.

Butson, C.R., Cooper, S.E., Henderson, J.M., McIntyre, C.C., 2007. Patient-specific analysis of the volume of tissue activated during deep brain stimulation. Neuroimage 34, 661–670.

Chen, M., Mogul, D.J., 2009. A structurally detailed finite element human head model for simulation of transcranial magnetic stimulation. J. Neurosci. Methods 179, 111–120.

Datta, A., Elwassif, M., Battaglia, F., Bikson, M., 2008. Transcranial current stimulation focality using disc and ring electrode configurations: FEM analysis. J. Neural Eng. 5, 163–174.

Datta, A., Bansal, V., Diaz, J., Patel, J., Reato, D., Bikson, M., 2009. Gyri-precise head model of transcranial direct current stimulation: improved spatial focality using a ring electrode versus conventional rectangular pad. Brain Stimul. 2, 201–207.

De Lucia, M., Parker, G.J.M., Embleton, K., Newton, J.M., Walsh, V., 2007. Diffusion tensor MRI-based estimation of the influence of brain tissue anisotropy on the effects of transcranial magnetic stimulation. Neuroimage 36, 1159–1170.

Deng, Z.D., Lisanby, S.H., Peterchev, A.V., 2009. Effect of anatomical variability on neural stimulation strength and focality in electroconvulsive therapy (ECT) and magnetic seizure therapy (MST). Conf. Proc. IEEE Eng. Med. Biol. Soc. 1, 682–688.

Deng, Z.D., Lisanby, S.H., Peterchev, A.V., 2010. Improving the focality of electroconvulsive therapy: the roles of current amplitude, and electrode size and spacing. J. ECT 26 (2), 151.

Deng, Z.D., Lisanby, S.H., Peterchev, A.V., 2011. Electric field strength and focality in electroconvulsive therapy and magnetic seizure therapy: a finite element simulation study. J. Neural Eng. 8, 016007.

Dmochowski, J.P., Bikson, M., Datta, A., Su, Y., Parra, L.C., 2011. A multiple electrode scheme for optimal non-invasive electrical stimulation. 5th Int. IEEE/EMBS Conf. Neural Eng, pp. 29–35.

Dogdas, B., Shattuck, D.W., Leahy, R.M., 2005. Segmentation of skull and scalp in 3-D human MRI using mathematical morphology. Hum. Brain Mapp. 26, 273–285.

Drechsler, F., Wolters, C.H., Dierkes, T., Si, H., Grasedyck, L., 2009. A full subtraction approach for finite element method based source analysis using constrained Delaunay tetrahedralisation. Neuroimage 46, 1055–1065.
Fitzgerald, P.B., Daskalakis, Z.J., 2011. The effects of repetitive transcranial magnetic stimulation in the treatment of depression. Expert Rev. Med. Devices 8, 85–95.
Fuchs, M., Wagner, M., Kastner, J., 2007. Development of volume conductor and source models to localize epileptic foci. J. Clin. Neurophysiol. 24, 101–119.
Geddes, L., Baker, L., 1967. The specific resistance of biological material. A compendium of data for the biomedical engineer and physiologist. Med. Biol. Eng. 5, 271–293.
Goldstein, J.M., Seidman, L.J., Makris, N., Ahern, T., O'Brien, L.M., Caviness, V.S., Kennedy, D.N., Faraone, S.V., Tsuang, M.T., 2007. Hypothalamic abnormalities in schizophrenia: sex effects and genetic vulnerability. Biol. Psychiatry 61, 935–945.
Grandori, F., Rossini, P., 1988. Electrical stimulation of the motor cortex: theoretical considerations. Ann. Biomed. Eng. 16, 639–652.
Guillery, R.W., Sherman, S.M., 2002. Thalamic relay functions and their role in corticocortical communication: generalizations from the visual system. Neuron 33, 163–175.
Gullmar, D., Haueisen, J., Eiselt, M., Giessler, F., Flemming, L., Anwander, A., Knoesche, T.R., Wolters, C.H., Dumpelmann, M., Tuch, D.S., Reichenbach, J.R., 2006. Influence of anisotropic conductivity on EEG source reconstruction: investigations in a rabbit model. IEEE Trans. Biomed. Eng. 53, 1841–1850.
Gullmar, D., Haueisen, J., Reichenbach, J.R., 2010. Influence of anisotropic electrical conductivity in white matter tissue on the EEG/MEG forward and inverse solution. a high-resolution whole head simulation study. Neuroimage 51, 145–163.
Gutman, D.A., Holtzheimer, P.E., Behrens, T.E.J., Johansen-Berg, H., Mayberg, H.S., 2009. A tractography analysis of two deep brain stimulation white matter targets for depression. Biol. Psychiatry 65, 276–282.
Hallez, H., Vanrumste, B., Van Hese, P., Delputte, S., Lemahieu, I., 2008. Dipole estimation errors due to differences in modeling anisotropic conductivities in realistic head models for EEG source analysis. Phys. Med. Biol. 53, 1877–1894.
Hallez, H., Staelens, S., Lemahieu, I., 2009. Dipole estimation errors due to not incorporating anisotropic conductivities in realistic head models for EEG source analysis. Phys. Med. Biol. 54, 6079–6093.
Haueisen, J., Tuch, D.S., Ramon, C., Schimpf, P.H., Wedeen, V.J., George, J.S., Belliveau, J.W., 2002. The influence of brain tissue anisotropy on human EEG and MEG. Neuroimage 15, 159–166.
Holdefer, R.N., Sadleir, R., Russell, M.J., 2006. Predicted current densities in the brain during transcranial electrical stimulation. Clin. Neurophysiol. 117, 1388–1397.
Im, C.H., Jung, H.H., Choi, J.D., Lee, S.Y., Jung, K.Y., 2008. Determination of optimal electrode positions for transcranial direct current stimulation (tDCS). Phys. Med. Biol. 53, N219–N225.
Johansen-Berg, H., Gutman, D.A., Behrens, T.E.J., Matthews, P.M., Rushworth, M.F.S., Katz, E., Lozano, A.M., Mayberg, H.S., 2008. Anatomical connectivity of the subgenual cingulate region targeted with deep brain stimulation for treatment-resistant depression. Cereb. Cortex 18, 1374–1383.
John, J.P., Yashavantha, B.S., Gado, M., Veena, R., Jain, S., Ravishankar, S., Csernansky, J.G., 2007. A proposal for MRI-based parcellation of the frontal pole. Brain Struct. Funct. 212, 245–253.
Kellner, C.H., Knapp, R., Husain, M.M., Rasmussen, K., Sampson, S., Cullum, M., McClintock, S.M., Tobias, K.G., Martino, C., Mueller, M., Bailine, S.H., Fink, M., Petrides, G., 2010a. Bifrontal, bitemporal and right unilateral electrode placement in ECT: randomised trial. Br. J. Psychiatry 196, 226–234.
Kellner, C.H., Tobias, K.G., Wiegand, J., 2010b. Electrode placement in electroconvulsive therapy (ECT): a review of the literature. J. ECT 26, 175–180.
Kim, S., Kim, T.S., Zhou, Y.X., Singh, M., 2003. Influence of conductivity tensors on the scalp electrical potential: study with 2-D finite element models. IEEE Trans. Nucl. Sci. 50, 133–139.
Klepfer, R.N., Johnson, C.R., Macleod, R.S., 1997. The effects of inhomogeneities and anisotropies on electrocardiographic fields: a 3-D finite-element study. IEEE Trans. Biomed. Eng. 44, 706–719.
Korgaonkar, M.S., Grieve, S.M., Koslow, S.H., Gabrieli, J.D., Gordon, E., Williams, L.M., 2011. Loss of white matter integrity in major depressive disorder: evidence using tract-based spatial statistical analysis of diffusion tensor imaging. Hum. Brain Mapp. doi. org/10.1002/hbm.21178.
Krystal, A.D., Weiner, R.D., 1994. ECT seizure therapeutic adequacy. Convuls. Ther. 10, 153–164.
Krystal, A.D., Weiner, R.D., McCall, W.V., Shelp, F.E., Arias, R., Smith, P., 1993. The effects of ECT stimulus dose and electrode placement on the ictal electroencephalogram: an intraindividual crossover study. Biol. Psychiatry 34, 759–767.
Lee, W.H., Kim, T.S., Cho, M.H., Ahn, Y.B., Lee, S.Y., 2006. Methods and evaluations of MRI content-adaptive finite element mesh generation for bioelectromagnetic problems. Phys. Med. Biol. 51, 6173–6186.
Lee, W.H., Kim, T.S., Kim, A.T., Lee, S.Y., 2008. 3-D diffusion tensor MRI anisotropy content-adaptive finite element head model generation for bioelectromagnetic imaging. Conf. Proc. IEEE Eng. Med. Biol. Soc. 4003–4006.
Lee, W.H., Liu, Z.M., Mueller, B.A., Lim, K., He, B., 2009a. Influence of white matter anisotropic conductivity on EEG source localization: comparison to fMRI in human primary visual cortex. Clin. Neurophysiol. 120, 2071–2081.
Lee, W.H., Seo, H.S., Kim, S.H., Cho, M.H., Lee, S.Y., Kim, T.S., 2009b. Influence of white matter anisotropy on the effects of transcranial direct current stimulation: a finite element study. Int. Conf. Biomed. Eng. 460–464.
Lee, W.H., Deng, Z.D., Kim, T.S., Laine, A.F., Lisanby, S.H., Peterchev, A.V., 2010. Regional electric field induced by electroconvulsive therapy: a finite element simulation study. Conf. Proc. IEEE Eng. Med. Biol. Soc. 1, 2045–2048.
Lee, W.H., Deng, Z.D., Laine, A.F., Lisanby, S.H., Peterchev, A.V., 2011. Influence of white matter conductivity anisotropy on electric field induced by electroconvulsive therapy. Conf. Proc. IEEE Eng. Med. Biol. Soc. 1, 5473–5476.
Lisanby, S.H., Maddox, J.H., Prudic, J., Devanand, D.P., Sackeim, H.A., 2000. The effects of electroconvulsive therapy on memory of autobiographical and public events. Arch. Gen. Psychiatry 57, 581–590.
Loo, C., Stewart, P., MacPherson, R., Hadzi-Pavlovic, D., 2009. Lower incidence of asystole and bradycardia with ultrabrief pulsewidth stimulation and bifrontal electrode placement. J. ECT 25, 149–150.
Lorimer, F.M., Segal, M.M., Stein, S.N., 1949. Path of current distribution in brain during electro-convulsive therapy; preliminary report. Electroencephalogr. Clin. Neurophysiol. 1, 343–348.
Luber, B., Nobler, M.S., Moeller, J.R., Katzman, G.P., Prudic, J., Devanand, D.P., Dichter, G.S., Sackeim, H.A., 2000. Quantitative EEG during seizures induced by electroconvulsive therapy: relations to treatment modality and clinical features. II. Topographic analyses. J. ECT 16, 229–243.
Makris, N., Meyer, J.W., Bates, J.F., Yeterian, E.H., Kennedy, D.N., Caviness, V.S., 1999. MRI-based topographic parcellation of human cerebral white matter and nuclei II. Rationale and applications with systematics of cerebral connectivity. Neuroimage 9, 18–45.
Marin, G., Guerin, C., Baillet, S., Garnero, L., Meunier, G., 1998. Influence of skull anisotropy for the forward and inverse problem in EEG: simulation studies using FEM on realistic head models. Hum. Brain Mapp. 6, 250–269.
Mayberg, H.S., 2009. Targeted electrode-based modulation of neural circuits for depression. J. Clin. Invest. 119, 717–725.
Mayberg, H.S., Lozano, A.M., Voon, V., McNeely, H.E., Seminowicz, D., Hamani, C., Schwalb, J.M., Kennedy, S.H., 2005. Deep brain stimulation for treatment-resistant depression. Neuron 45, 651–660.
McCormick, L.M., Ziebell, S., Nopoulos, P., Cassell, M., Andreasen, N.C., Brumm, M., 2006. Anterior cingulate cortex: an MRI-based parcellation method. Neuroimage 32, 1167–1175.
McNally, K.A., Blumenfeld, H., 2004. Focal network involvement in generalized seizures: new insights from electroconvulsive therapy. Epilepsy Behav. 5, 3–12.
McNeely, H.E., Mayberg, H.S., Lozano, A.M., Kennedy, S.H., 2008. Neuropsychological impact of Cg25 deep brain stimulation for treatment-resistant depression: preliminary results over 12 months. J. Nerv. Ment. Dis. 196, 405–410.
Miranda, P.C., Lomarev, M., Hallett, M., 2006. Modeling the current distribution during transcranial direct current stimulation. Clin. Neurophysiol. 117, 1623–1629.
Miranda, P.C., Correia, L., Salvador, R., Basser, P.J., 2007. Tissue heterogeneity as a mechanism for localized neural stimulation by applied electric fields. Phys. Med. Biol. 52, 5603–5617.
Nadeem, M., Thorlin, T., Gandhi, O.P., Persson, M., 2003. Computation of electric and magnetic stimulation in human head using the 3-D impedance method. IEEE Trans. Biomed. Eng. 50, 900–907.
Nagler, J., 2010. Absence of asystole during bifrontal stimulation in electroconvulsive therapy. J. ECT 26, 100–103.
Nakamura, M., Nestor, P.G., Levitt, J.J., Cohen, A.S., Kawashima, T., Shenton, M.E., McCarley, R.W., 2008. Orbitofrontal volume deficit in schizophrenia and thought disorder. Brain 131, 180–195.
Nathan, S.S., Sinha, S.R., Gordon, B., Lesser, R.P., Thakor, N.V., 1993. Determination of current-density distributions generated by electrical-stimulation of the human cerebral-cortex. Electroencephalogr. Clin. Neurophysiol. 86, 183–192.
Nicholson, P.W., 1965. Specific impedance of cerebral white matter. Exp. Neurol. 13, 386–401.
Nuttall, G.A., Bowersox, M.R., Douglass, S.B., McDonald, J., Rasmussen, L.J., Decker, P.A., Oliver, W.C., Rasmussen, K.G., 2004. Morbidity and mortality in the use of electroconvulsive therapy. J. ECT 20, 237–241.
Oostendorp, T.F., Hengeveld, Y.A., Wolters, C.H., Stinstra, J., van Elswijk, G., Stegeman, D.F., 2008. Modeling transcranial DC stimulation. Conf. Proc. IEEE Eng. Med. Biol. Soc. , pp. 4226–4229.
Oppenheimer, S., 2006. Cerebrogenic cardiac arrhythmias: cortical lateralization and clinical significance. Clin. Auton. Res. 16, 6–11.
Oppenheimer, S.M., Gelb, A., Girvin, J.P., Hachinski, V.C., 1992. Cardiovascular effects of human insular cortex stimulation. Neurology 42, 1727–1732.
Ottosson, J.O., 1960. Experimental studies of memory impairment after electroconvulsive therapy. the role of the electrical stimulation and of the seizure studied by variation of stimulus intensity and modification by lidocaine of seizure discharge. Acta Psychiatr. Scand. Suppl. 35, 103–131.
Parazzini, M., Fiocchi, S., Rossi, E., Paglialonga, A., Ravazzani, P., 2011. Transcranial direct current stimulation: estimation of the electric field and of the current density in an anatomical human head model. IEEE Trans. Biomed. Eng. 58, 1773–1780.
Park, J.H., Hong, S.B., Kim, D.W., Suh, M., Im, C.H., 2011. A novel array-type transcranial direct current stimulation (tDCS) system for accurate focusing on targeted brain areas. IEEE Trans. Magn. 47, 882–885.
Peterchev, A.V., Rosa, M.A., Deng, Z.D., Prudic, J., Lisanby, S.H., 2010. Electroconvulsive therapy stimulus parameters: rethinking dosage. J. ECT 26, 159–174.
Plonsey, R., Heppner, D.B., 1967. Considerations of quasi-stationarity in electrophysiological systems. Bull. Math. Biophys. 29, 657–664.
Pons, J.P., Segonne, E., Boissonnat, J.D., Rineau, L., Yvinec, M., Keriven, R., 2007. High-quality consistent meshing of multi-label datasets. Inf. Process. Med. Imaging 20, 198–210.
Radman, T., Ramos, R.L., Brumberg, J.C., Bikson, M., 2009. Role of cotical cell type and morphology in subthreshold and suprathreshold uniform electric field sitmulation *in vitro*. Brain Stimul. 2, 215–228.
Rampersad, S., Stegeman, D., Oostendorp, T., 2011. On handling the layered structure of the skull in transcranial direct current stimulation models. Conf. Proc. IEEE Eng. Med. Biol. Soc. 1989–1992.
Ranta, M.E., Crocetti, D., Clauss, J.A., Kraut, M.A., Mostofsky, S.H., Kaufmann, W.E., 2009. Manual MRI parcellation of the frontal lobe. Psychiatry Res. 172, 147–154.

Rattay, F., 1988. Modeling the excitation of fibers under surface electrodes. IEEE Trans. Biomed. Eng. 35, 199–202.
Rullmann, M., Anwander, A., Dannhauer, M., Warfield, S.K., Duffy, F.H., Wolters, C.H., 2009. EEG source analysis of epileptiform activity using a 1 mm anisotropic hexahedra finite element head model. Neuroimage 44, 399–410.
Rush, S., Driscoll, D.A., 1968. Current distribution in brain from surface electrodes. Anesth. Analg. 47, 717–723.
Rushton, W.A.H., 1927. The effect upon the threshold for nervous excitation of the length of nerve exposed, and the angle between current and nerve. J. Physiol. 9, 357–377.
Sackeim, H.A., 2004. Convulsant and anticonvulsant properties of electroconvulsive therapy: towards a focal form of brain stimulation. Clin. Neurosci. Res. 4, 39–57.
Sackeim, H.A., Mukherjee, S., 1986. Neurophysiological variability in the effects of the ECT stimulus. Convuls. Ther. 2, 267–276.
Sackeim, H.A., Prudic, J., Devanand, D.P., Decina, P., Kerr, B., Malitz, S., 1990. The impact of medication resistance and continuation pharmacotherapy on relapse following response to electroconvulsive therapy in major depression. J. Clin. Psychopharmacol. 10, 96–104.
Sackeim, H.A., Devanand, D.P., Prudic, J., 1991. Stimulus intensity, seizure threshold, and seizure duration: impact on the efficacy and safety of electroconvulsive therapy. Psychiatr. Clin. North Am. 14, 803–843.
Sackeim, H.A., Prudic, J., Devanand, D.P., Nobler, M.S., Lisanby, S.H., Peyser, S., Fitzsimons, L., Moody, B.J., Clark, J., 2000. A prospective, randomized, double-blind comparison of bilateral and right unilateral electroconvulsive therapy at different stimulus intensities. Gen. Psychiatry 57, 425–434.
Sackeim, H.A., Prudic, J., Fuller, R., Keilp, J., Lavori, P.W., Olfson, M., 2007. The cognitive effects of electroconvulsive therapy in community settings. Neuropsychopharmacology 32, 244–254.
Sackeim, H.A., Prudic, J., Nobler, M.S., Fitzsimons, L., Lisanby, S.H., Payne, N., Berman, R.M., Brakerneier, E.L., Perera, T., Devanand, D.P., 2008. Effects of pulse width and electrode placement on the efficacy and cognitive effects of electroconvulsive therapy. Brain Stimul. 1, 71–83.
Sadleir, R.J., Argibay, A., 2007. Modeling skull electrical properties. Ann. Biomed. Eng. 35, 1699–1712.
Sadleir, R.J., Vannorsdall, T.D., Schretlen, D.J., Gordon, B., 2010. Transcranial direct current stimulation (tDCS) in a realistic head model. Neuroimage 51, 1310–1318.
Salvador, R., Mekonnen, A., Ruffini, G., Miranda, P.C., 2010. Modeling the electric field induced in a high resolution realistic head model during transcranial current stimulation. Conf. Proc. IEEE Eng. Med. Biol. Soc. 1, 2073–2076.
Saypol, J.M., Roth, B.J., Cohen, L.G., Hallett, M., 1991. A theoretical comparison of electric and magnetic stimulation of the brain. Ann. Biomed. Eng. 19, 317–328.
Sekino, M., Ueno, S., 2002. Comparison of current distributions in electroconvulsive therapy and transcranial magnetic stimulation. J. Appl. Phys. 91, 8730–8732.
Sekino, M., Ueno, S., 2004. FEM-based determination of optimum current distribution in transcranial magnetic stimulation as an alternative to electroconvulsive therapy. IEEE Trans. Magn. 40, 2167–2169.
Shattuck, D.W., Leahy, R.M., 2002. BrainSuite: an automated cortical surface identification tool. Med. Image Anal. 6, 129–142.
Shimony, J.S., McKinstry, R.C., Akbudak, E., Aronovitz, J.A., Snyder, A.Z., Lori, N.F., Cull, T.S., Conturo, T.E., 1999. Quantitative diffusion-tenser anisotropy brain MR imaging: normative human data and anatomic analysis. Radiology 212, 770–784.
Smitt, J.W., Wegener, C.F., 1944. On electric convulsive therapy with particular regard to a parietal application of electrodes, controlled by intracerebral voltage measurements. Acta Psychiatr. Neurol. 19, 529–549.
Spellman, T., Peterchev, A.V., Lisanby, S.H., 2009. Focal electrically administered seizure therapy: a novel form of ECT illustrates the roles of current directionality, polarity, and electrode configuration in seizure induction. Neuropsychopharmacology 34, 2002–2010.
Squire, L.R., 1986. Memory functions as affected by electroconvulsive-therapy. Ann. N. Y. Acad. Sci. 462, 307–314.
Squire, L.R., Slater, P.C., Miller, P.L., 1981. Retrograde-amnesia and bilateral electroconvulsive-therapy-long-term follow-up. Gen. Psychiatry 38, 89–95.
Stecker, M.M., 2005. Transcranial electric stimulation of motor pathways: a theoretical analysis. Comput. Biol. Med. 35, 133–155.
Suh, H.S., Kim, S.H., Lee, W.H., Kim, T.S., 2009. Realistic simulation of transcranial direct current stimulation via 3-D high-resolution finite element analysis: effect of tissue anisotropy. Conf. Proc. IEEE Eng. Med. Biol. Soc. 638–641.
Suh, H.S., Lee, W.H., Cho, Y.S., Kim, J.H., Kim, T.S., 2010. Reduced spatial focality of electrical field in tDCS with ring electrodes due to tissue anisotropy. Conf. Proc. IEEE Eng. Med. Biol. Soc. 1, 2053–2056.
Suihko, V., 2002. Modelling the response of scalp sensory receptors to transcranial electrical stimulation. Med. Biol. Eng. Comput. 40, 395–401.
Szmurło, R., Sawicki, B., Starzynski, J., Wincenciak, S., 2006. A comparison of two models of electrodes for ECT simulations. IEEE Trans. Magn. 42, 1395–1398.
Thielscher, A., Opitz, A., Windhoff, M., 2011. Impact of the gyral geometry on the electric field induced by transcranial magnetic stimulation. Neuroimage 54, 234–243.
Tsopelas, C., Stewart, R., Savva, G.M., Brayne, C., Ince, P., Thomas, A., Matthews, F.E., 2011. Neuropathological correlates of late-life depression in older people. Br. J. Psychiatry 198, 109–114.
Tu, Z., Narr, K.L., Dollar, P., Dinov, I., Thompson, P.M., Toga, A.W., 2008. Brain anatomical structure segmentation by hybrid discriminative/generative models. IEEE Trans. Med. Imaging 27, 495–508.
Tuch, D.S., Wedeen, V.J., Dale, A.M., George, J.S., Belliveau, J.W., 1999. Conductivity mapping of biological tissue using diffusion MRI. Ann. N. Y. Acad. Sci. 888, 314–316.
Tuch, D.S., Wedeen, V.J., Dale, A.M., George, J.S., Belliveau, J.W., 2001. Conductivity tensor mapping of the human brain using diffusion tensor MRI. Proc. Natl. Acad. Sci. U.S.A. 98, 11697–11701.
Wagner, T., Fregni, F., Fecteau, S., Grodzinsky, A., Zahn, M., Pascual-Leone, A., 2007. Transcranial direct current stimulation: a computer-based human model study. Neuroimage 35, 1113–1124.
Wang, K., Zhu, S., Mueller, B.A., Lim, K.O., Liu, Z.M., He, B., 2008. A new method to derive white matter conductivity from diffusion tensor MRI. IEEE Trans. Biomed. Eng. 55, 2481–2486.
Weaver, L., Williams, R., Rush, S., 1976. Current density in bilateral and unilateral ECT. Biol. Psychiatry 11, 303–312.
Weiss, A.P., DeWitt, I., Goff, D., Ditman, T., Heckers, S., 2005. Anterior and posterior hippocampal volumes in schizophrenia. Schizophr. Res. 73, 103–112.
Welch, C.A., Drop, L.J., 1989. Cardiovascular effects of ECT. Convuls. Ther. 5, 35–43.
Wells 3rd, W.M., Viola, P., Atsumi, H., Nakajima, S., Kikinis, R., 1996. Multi-modal volume registration by maximization of mutual information. Med. Image Anal. 1, 35–51.
Wible, C.G., Shenton, M.E., Fischer, I.A., Allard, J.E., Kikinis, R., Jolesz, F.A., Iosifescu, D.V., McCarley, R.W., 1997. Parcellation of the human prefrontal cortex using MRI. Psychiatry Res. 76, 29–40.
Wolters, C.H., Anwander, A., Tricoche, X., Weinstein, D., Koch, M.A., MacLeod, R.S., 2006. Influence of tissue conductivity anisotropy on EEG/MEG field and return current computation in a realistic head model: a simulation and visualization study using high-resolution finite element modeling. Neuroimage 30, 813–826.
Wu, F., Tang, Y., Xu, K., Kong, L., Sun, W., Wang, F., Kong, D., Li, Y., Liu, Y., 2011. White matter abnormalities in medication-naive subjects with a single short-duration episode of major depressive disorder. Psychiatry Res. 191, 80–83.